Facile and Versatile Sol−Gel Strategy for the Preparation of a High-Loaded ZnO/SiO$_2$ Adsorbent for Room-Temperature H$_2$S Removal

Chao Yang,[†] Jiawei Kou,[†] Huiling Fan,*,[†] Zhen Tian,[‡] Wei Kong,[§] and Ju Shangguan[†]

[†]State Key Laboratory of Coal Science and Technology, Co-founded by Shanxi Province and the Ministry of Science and Technology, and [§]Department of Chemical Engineering, Taiyuan University of Technology, West Yingze Street Number 79, Taiyuan 030024, People's Republic of China

[‡]Deparment of Analysis and Service Center, Micromeritics Instrumental Ltd, Shanghai 1071, China

ABSTRACT: Preparation of well-dispersed ZnO nanograins is necessary to improve their reactivity toward room-temperature H$_2$S removal. However, the challenge to design such a ZnO-based adsorbent with high ZnO loading is yet to be fulfilled. Herein, a facile sol−gel strategy is reported for the preparation of ZnO/SiO$_2$ adsorbents for efficient H$_2$S removal, by innovating a gel-drying method and simultaneously controlling ZnO grain formation through optimizing the molar ratio of ethylene glycol (EG)/nitrates in its precursors. The fabricated adsorbent embedded well-dispersed ZnO nanograins, of approximately 10−15 nm, into a SiO$_2$ matrix (57 wt % ZnO loading) and thus yielded a high H$_2$S removal capacity of 108.9 mg S/g sorbent. Therein, EG was used as a modifier for inhibiting the formation of a denser SiO$_2$ network during the gel drying process and was used as a fuel for promoting the decomposition of nitrates and increasing the surface area of the composites in the subsequent calcination.

Modulating the molar ratio of EG/nitrates ≤ 2 in precursors or traditional drying of the gel in an oven should be avoided because these would lead to the oxidation of EG by metallic nitrates and form carboxylate complexes during the gel-drying process. Although the produced ZnO grains had a very small size of less than 5 nm, a layer of monodentate ZnCO$_3$ impurity was formed on the ZnO surface, which will drastically decrease the reactivity of ZnO toward H$_2$S. According to the encouraging results from CuO and Co$_3$O$_4$, this strategy has proved to be versatile for the preparation of other metal oxide/SiO$_2$ adsorbents.
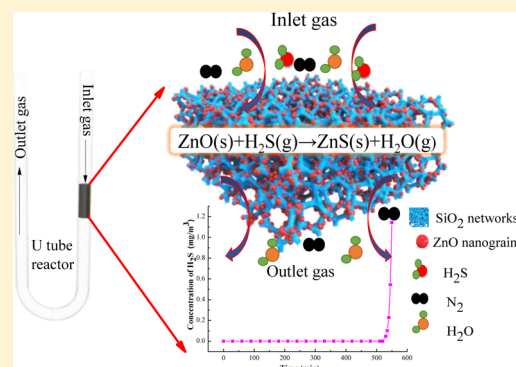
INTRODUCTION

Proton exchange membrane fuel cells (PEMFCs), as a green power source, show great potential for residential and industrial applications.[1,2] However, the performance of PEMFCs deteriorates when hydrogen fuel is contaminated with impurities such as H$_2$S, CO, and CO$_2$.[1] The effects of these impurities can contribute to three negative consequences: (1) poisoning electrocatalysts, which lead to kinetic losses; (2) increasing the resistance of cell components, which result in ohmic losses; and (3) transmuting the structure and hydrophobicity of components, which yield mass transport losses.[2−5] H$_2$S, which is more poisonous than CO toward the performance of PEMFCs, can drastically damage electrocatalysts even at concentrations as low as 0.1 ppm.[2,6−8] Therefore, lowering the H$_2$S content to below 0.1 ppm in hydrogen fuels at room temperature is critical to improving the durability and reliability of PEMFCs. Zinc oxide, which has very favorable thermodynamics toward sulfidation reactions, is widely used to remove H$_2$S.[9−12] However, conventional bulk ZnO-based sorbents possess very low sulfur capacity at room temperature due to the kinetic limitations.[13]

Compared to bulk ZnO, nanoscale ZnO grains are advantageous due to quantum size effects, which can compensate for the slow sulfidation kinetics and reinstate ZnO as a prospect for room-temperature H$_2$S removal.[14] Consequently, various strategies have been developed to prepare nanoscale ZnO-based adsorbents. The prevailing method is to embed ZnO into porous materials (e.g., carbon-based and mesoporous sieves) by impregnation methods. This strategy can be easily implemented but with minimal ZnO content, that is, below 30 wt %, which normally yields an unsatisfactory sulfur capacity of less than 50 mg S/g sorbent.[15] In our previous work, a colloidal crystal template method was employed to prepare zinc oxide−silica composite adsorbents with three-dimensionally ordered macroporous structures.[11] The amorphous SiO$_2$ matrix promoted greater dispersibility of ZnO grains and confined 50 wt % more ZnO within its pores. Moreover, the interconnected hierarchical pore structure reduced the mass transfer resistance during desulfurization. Therefore, the obtained sulfur capacity of the sorbents was able to reach an impressive 135 mg S/g sorbent. However, this preparation process is complex and tedious. Therefore, a facile preparation strategy, which can synthesize

ZnO-based adsorbents with high ZnO loadings, nanoscale ZnO grains, and high sulfur capacity, is urgently needed.

The sol−gel method, which could prepare composites with a homogenous distribution of nanoscale particles, has been widely used in catalyst preparation.[16−18] Recently, sol−gel strategies have also been designed for preparing ZnO-based sorbents for H_2S removal, yielding notable results.[9,19] For examples, Polychronopoulou et al. prepared a series of novel ZnO/TiO_2 adsorbents with titanium isopropoxide and $(CH_3COO)_2Zn$ as the Ti and Zn sources, respectively. The H_2S uptake was measured at 51 mg S/g sorbent when the ZnO loading was 40 wt %; an even higher 80 mg S/g sorbent was noted after modifications.[20,21] Liu et al. fabricated ZnO/SiO_2 nanocomposites, the optimal ZnO loading content was 30 wt %, and the H_2S removal capacity was 91 mg S/g sorbent.[9]

Recently, a new sol−gel method was successfully developed using ethylene glycol (EG), metallic nitrates, and tetraethylorthosilicate (TEOS) as precursors to synthesize magnetic materials, $(Ni−Zn)Fe_2O_4/SiO_2$ and $Ni−ZnO/SiO_2$ nanocomposites. The obtained ferrites were ultrafine spherical nanoparticles (4−6 nm) that were homogeneously dispersed in a SiO_2 matrix with loadings up to 35 wt %.[22,23] Therein, EG was used as the reductant for the metallic nitrates to form a stable carboxylate complex through a redox reaction during the gel-drying process. The formed carboxylate complex could effectively inhibit the agglomeration of metal oxides because of its high decomposition temperature.[24,25]

In this paper, a facile sol−gel strategy using EG, metallic nitrates, and TEOS as precursors was also reported to prepare ZnO/SiO_2 adsorbents for efficient H_2S removal. Differing from EG being utilized as a reductant, two new roles were observed via innovating the gel-drying method and modulating the molar ratio of EG/nitrates in the precursor in the new developed sol−gel strategy. First, EG was used as a modifier during the gel drying process to form developed mesoporous SiO_2 networks, which, in turn aid the dispersing of ZnO nanograins. Second, EG was being used as fuel to promote the decomposition of nitrates and increase the surface area of the composites during calcination. As a result, well-dispersed ZnO nanograins (10−15 nm) with loadings of up to 57 wt % were embedded into the SiO_2 matrix. More importantly, a satisfactory H_2S removal capacity of 108.9 mg S/g sorbent was achieved. On modulating the molar ratio of EG/nitrates to less than 2 in precursors or adopting the reported drying method, EG, as reported,[22] was oxidized by metallic nitrates to form a carboxylate complex during the gel drying process. However, although the produced ZnO grains were very small (below 5 nm), a by-product layer of monodentate $ZnCO_3$ would be formed on the ZnO surface, which significantly decreased the reactivity of ZnO toward H_2S. Additionally, according to the encouraging results from the fabricated sorbents, CuO/SiO_2 and Co_3O_4/SiO_2, this method was proven efficient and versatile for preparing other high-loaded metal oxide/silica adsorbents.

■ EXPERIMENTAL SECTION

Sorbent Preparation. All chemicals used were of analytical grade and commercially available. The desired ZnO/SiO_2 sorbents were synthesized by the sol−gel method.

Typically, anhydrous ethanol (EtOH), H_2O, and HNO_3 were added sequentially to TEOS at a molar ratio of 3:1.8:0.03:1 and stirred for 1 h to obtain a clear SiO_2 sol. Zinc nitrate was dissolved in EG at different molar ratios, and methanol was added to get zinc

nitrate solution with concentration of 2 M. The zinc nitrate solution was then added to the SiO_2 sol and stirred for another 1 h. The mixed solution was innovatively aged at 30 °C for 10 h and dried at 120 °C overnight in a closed chamber to form a gel, which we will herein term innovative drying. The gels were finally calcined in air initially at 300 °C for 2 h, then elevated at a rate of 1 °C/min up to and held at 500 °C for an additional 2 h. The schematic of the procedure is depicted in Scheme 1. For comparison with ref 22, a sample with a molar ratio

Scheme 1. Schematic Illustration for the Preparation of ZnO/SiO_2 Sorbents
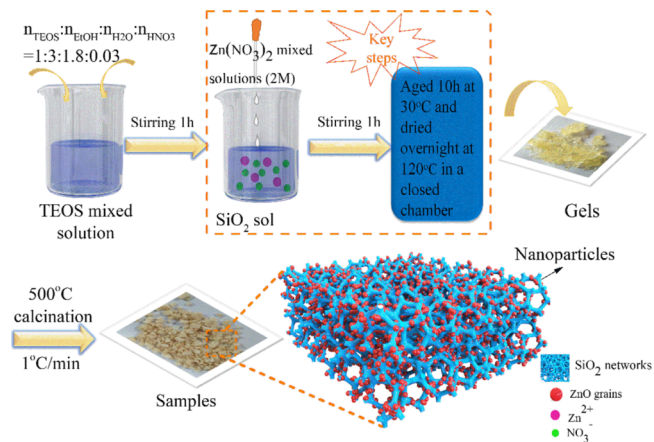
of EG/nitrates = 3:1 in the precursors was prepared by transferring the solution in oven, then aged at 30 °C for 10 h and dried at 120 °C overnight to form a gel, which was called traditional drying. The detailed molar compositions of the components are listed in Table 1.

Table 1. Composition of the Synthesized Gels

samples	composition in precursors (mol)			drying methods
	$Zn(NO_3)_2$	EG	methanol	
ZS-3-C	0.04	0.12	0.20	conventional drying
ZS-3	0.04	0.12	0.20	innovative drying
ZS-0.5	0.04	0.02	0.45	innovative drying
ZS-1	0.04	0.04	0.40	innovative drying
ZS-2	0.04	0.08	0.30	innovative drying
ZS-5	0.04	0.2	0	innovative drying

The fabricated gels before calcination will be denoted as ZS-XG and ZS-XG-C, and the sorbents after calcination will be shortened to ZS-X and ZS-X-C, where ZS refers to ZnO and SiO_2; X is the molar ratio of EG/nitrates; G is the abbreviation of the gels; and C is indexed to conventional drying.

The CuO/SiO_2 and Co_3O_4/SiO_2 nanocomposites were also synthesized with only the type of metallic nitrates changed relative to that of the sample ZS-3 to demonstrate the versatility of this method.

Characterizations of Material. The crystalline phases of the fabricated sorbents were determined on a Rigaku D/Max-2500 diffractometer with Cu $K\alpha$ radiation. The data between 5 and 80° were collected for wide-angle X-ray diffraction (XRD) studies (scanning rate = 8 °/min). The thermogravimetry experiments were performed on a thermal analyzer (Setaram SETSYS Evolution TGA) coupled with a mass spectrometer (Hiden HPR20 QIC R & D). The gels were heated up to 800 °C in air at a heating rate of 10 °C/min, and the air flow rate is 100 mL/min. The gas products were analyzed by the mass spectrometer. N_2 adsorption−desorption isotherms were measured at 77 K using a Nova 2000e instrument. The surface areas were calculated by the standard Brunauer−Emmett−Teller (BET) method, whereas the Barrett−Joyner−Halenda (BJH) model was used to calculate the pore size distributions (PSDs) and the total pore
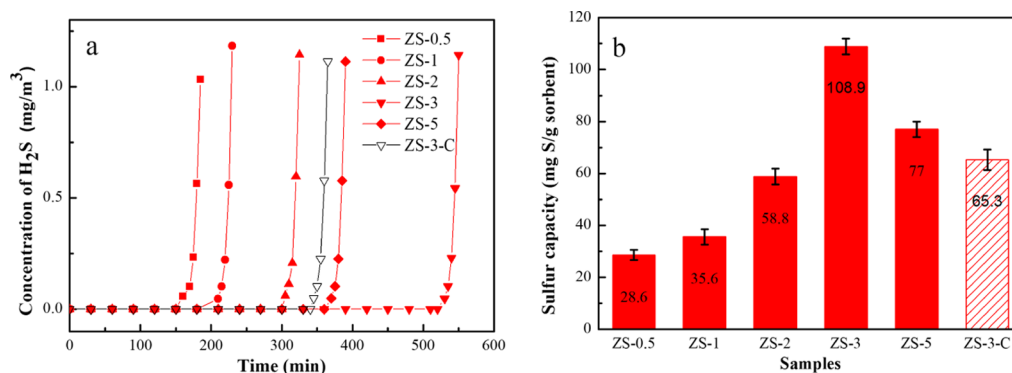
Figure 1. The breakthrough curves and the corresponding BSCs of the prepared samples.
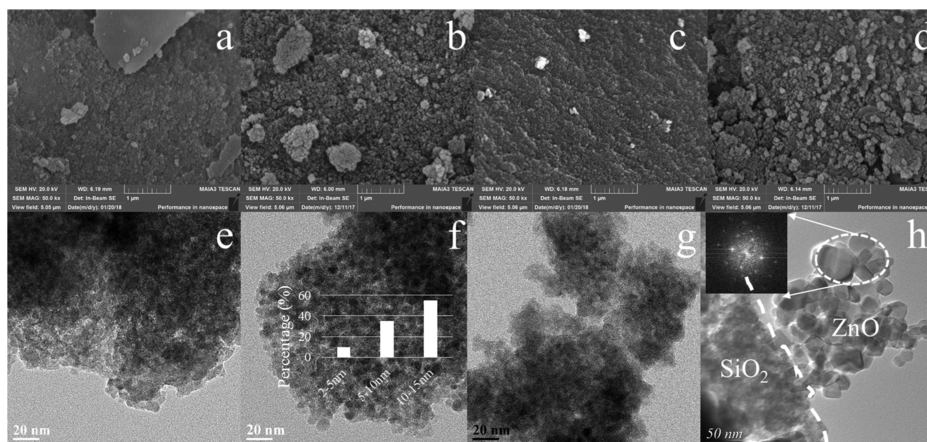

Figure 2. SEM and TEM images of samples ZS-3-C (a,e), ZS-3 (b,f), ZS-1 (c,g), and ZS-5 (d,h).

volumes. The Fourier transform infrared (FT-IR) spectra were studied on a 670 FT-IR spectrophotometer (Thermo Nicolet, USA) (600−4000 cm^{-1}). The morphology of sorbents was collected on a NanoSEM430 scanning electron microscopy (SEM) and on a Tecnai G2F20 transmission electron microscopy (TEM). X-ray photoelectron spectroscopy (XPS) measurements were performed using an ESCALAB 250 spectrometer (VG Scientific Ltd., UK) equipped with a monochromated Al Kα source ($h\nu$ = 1486.6 eV, 150 W) and under ultrahigh vacuum (7 × 10^{-8} Pa). The binding energy was calibrated by the C 1s peak at 284.6 eV. UV−visible spectra were recorded on a PerkinElmer Lambda 9 UV/vis/NIR spectrophotometer equipped with a RSA-PE-19 biconical optical bench for diffuse reflectance measurement.

Performance Tests. The breakthrough tests of the prepared samples were evaluated on a fixed bed. The typical process involved initial grinding of the adsorbents into 40−60 mesh and loaded into a U-tube reactor (inner diameter 6 mm) with the loading height of 2 cm. Then, the loaded sorbents were prehumidified with moist N$_2$ (ca. 3% moisture) by bubbling N$_2$ in water at 30 °C for 1.5 h. Finally, H$_2$S with a concentration of 850 mg/m^3 in moist N$_2$ is passed through the U-tube reactor; the total flow rate was 100 mL/min. The inlet and outlet H$_2$S concentrations were detected by a gas chromatograph equipped with a flame photometric detector. The tests were completed when the outlet H$_2$S concentration exceeds 0.15 mg/m^3, and the sulfur capacity of the sorbent can be calculated by integrating the breakthrough curves area.

■ RESULT AND DISCUSSION

Desulfurization Performance. First, only considering the two adsorbents, ZC-3 and ZC-3-C in Figure 1a,b, which were prepared by different drying methods, both samples showed high removal precision with the concentration of H$_2$S in the

outlet below 0.08 ppm at the initial stage of reaction, however, the H$_2$S concentrations in the outlet increased dramatically after reaching the breakthrough, implying the fast kinetics of the adsorption process. ZS-3-C showed a breakthrough time (BT) of 350 min and a corresponding breakthrough sulfur capacity (BSC) of 63.5 mg S/g sorbent. Although ZS-3 showed a prolonged BT of 535 min, the sulfur capacity was 108.9 mg S/g sorbent, which was almost 1.7 times that of ZS-3-C, demonstrating a significant influence on H$_2$S removal performance depending on drying methods.

Modulating the molar ratio of EG/nitrates in precursors also led to a variation in the sulfur capacity of the sorbent. For both lowering and increasing the EG content in precursors, the samples showed a decrease in sulfur capacity in comparison with sample ZS-3. Specifically, ZS-0.5 exhibited the shortest BT (168 min), and its corresponding BSC was only 28.6 mg S/g sorbent. In a nutshell, the H$_2$S removal performance of the prepared samples seriously relied on the drying methods and the molar ratio of EG/nitrates in precursors, and the sample ZS-3 demonstrated the highest sulfur capacity of 108.9 mg S/g sorbent.

Morphology Characterization. The morphology of the selected samples was studied and is shown in Figure 2. The SEM images show that the obtained bulk sorbents are the result of a large amount of nanoparticle agglomeration. Some mesoporous voids formed due to the irregular arrangement of nanoparticles. ZS-3-C (Figure 2a) showed smaller nanoparticles with a denser stack than that of ZS-3 (Figure 2b). According to the TEM results, the nanoparticles shown in the SEM images were composed of the ZnO grains and SiO$_2$
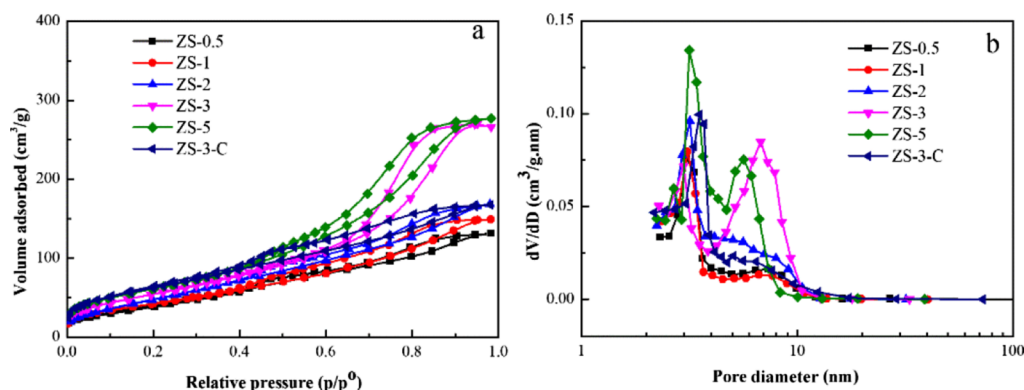
Figure 3. N$_2$ adsorption and desorption isotherms and PSDs of the samples.

networks. ZnO grains were embedded and well-dispersed in the SiO$_2$ matrix of both samples. However, ZS-3 showed larger ZnO grains compared to ZS-3-C, demonstrating that the drying methods have greatly affected the size of ZnO grains.

The SEM images also indicate that the size of nanoparticles varied depending on the molar ratio of EG/nitrates. Compared with ZS-3, a decrease in the nanoparticle size and a much denser stack among nanoparticles were observed when reducing the molar ratio of EG/nitrates. According to the TEM images, ZnO grains with smaller size in ZS-1 (Figure 2g) were also well dispersed in the SiO$_2$ matrix compared with that of ZS-3. Specifically, the size of ZnO grains averaged around 10−15 nm in ZS-3 (inserted in Figure 2f) based on the statistical results, whereas the average size was below 5 nm within ZS-1. Unlike ZS-1 and ZS-3, the ZnO grains in ZS-5 were partially isolated from the SiO$_2$ matrix as observed in Figure 2h. The size of the hexagonal ZnO grains was around 40 nm, which is far larger than those found in ZS-1 and ZS-3. This may be caused by the absence of methanol in the precursors of ZS-5, which led to an increase in terms of mixed sol viscosity and hindered the movement of Zn(NO$_3$)$_2$ into the SiO$_2$ matrix.

Texture Analysis. Figure 3 shows the N$_2$ adsorption desorption isotherms of the sorbents and PSDs. All samples reveal type IV isotherms accompanied with a typical H2 type hysteresis loop, affirming the mesoporous features within these materials.[26,27] Compared with ZS-3-C, ZS-3 showed a sharper increase in absorption when the relative pressure is in the range of 0.7−0.9, suggesting more mesopores and with larger pore sizes were uncovered in ZS-3. The PSD curves reveal that both samples exhibited a bimodal PSD, one centered at approximately 3 nm and the other was roughly at 8 nm. However, the majority of the pore sizes of ZS-3-C were measured at 3 nm, whereas those of ZS-3 were at 8 nm. The detailed textural properties are listed in Table 2. The specific surface area (SSA), V_t and W_{BJH} of ZS-3 are both larger than those of ZS-3-C.

ZS-0.5, ZS-1, and ZS-2 showed isotherms and PSDs similar to those of ZS-3-C, whereas ZS-5 was similar to ZS-3. As seen in Table 2, the SSA and V_t of all samples increased as the molar ratio of EG/nitrate increased. Moreover, ZS-5 was measured with the largest surface area and the V_t was about 2.2 times that of ZS-0.5. The differences in the texture properties of these samples were caused by SiO$_2$ networks, which were readily influenced by the addition amount of EG.[28] On one hand, EG could inhibit further condensation of Si−OH to a denser SiO$_2$ network.[28−30] On the other hand, EG could reduce the

Table 2. Texture Parameters of Samples Prepared with Different Molar Ratio of EG/Nitrates[a]

sample	S_{BET} (m^2/g)	V_t (cm^3/g)	W_{BJH} (nm)
ZS-3-C	148.5	0.33	3.52
ZS-3	153.3	0.41	7.30
ZS-0.5	106.3	0.20	3.49
ZS-1	118.4	0.24	3.50
ZS-2	144.1	0.29	3.52
ZS-5	168.5	0.43	6.23

[a]S_{BET}, BET specific area; V_t, total pore volume; W_{BJH}, pore size determined from BJH desorption data.

capillary force during the gel drying process, decreasing the crack of the gel, which helped develop the pore structure and increase the surface area.[31]

FT-IR and XRD Analysis. Figure 4a shows the FT-IR spectra of the prepared nanocomposites. All samples produced the SiO$_2$ characteristic adsorption bands at 800, 1080, and 1210 cm^{-1}, which correspond to the symmetric stretching vibrations of Si−O−Si in the SiO$_4$ tetrahedron, the symmetric Si−O−Si stretching mode, as well as the asymmetric vibrational stretching mode of Si−O$^-$, respectively.[9,32,33] In addition, the Si−OH band at 960 cm^{-1},[11] and the adsorption bands of −OH groups at 1610 cm^{-1} (deforming vibrations) and 3440 cm^{-1} (stretching vibrations)[34] were observed in all samples. Specifically, ZS-3-C and ZS-3 showed analogous spectra except at the wavenumber, 1430 cm^{-1}, which is related to the formation of monodentate carbonate species exhibiting O−C−O stretching frequencies.[35] This band clearly appeared in ZS-3-C, but disappeared in ZS-3 and ZS-5, and yet, it was also found in samples ZS-0.5, ZS-1, and ZS-2. In summary, using the conventional drying method or modulating the molar ratio of EG/nitrates $\leq$ 2 in the precursors could favor the formation of monodentate carbonates during calcination.

Figure 4b shows the XRD pattern of the samples. ZS-3 displayed the characteristic peaks of hexagonal wurtzite zinc oxide at 2θ = 31.5°, 34.2°, 36.0°, 47.3°, 56.4°, 62.7°, and 68.9°.[36] Poor crystallization properties of ZnO nanograins in sample ZS-3-C with a relatively wide diffraction peak was observed at 2$\theta \approx$ 35° in the XRD pattern; such phenomenon was also found in ZS-0.5, ZS-1, and ZS-2. ZS-5 showed more intensified diffraction peaks than those of ZS-3. As it is known, the intensity of the diffraction peak within an XRD pattern is related to the grain size of the crystal. Thus, the XRD pattern demonstrated that larger ZnO grains was developed in ZS-3 and ZS-5 in comparison to the other samples. This further
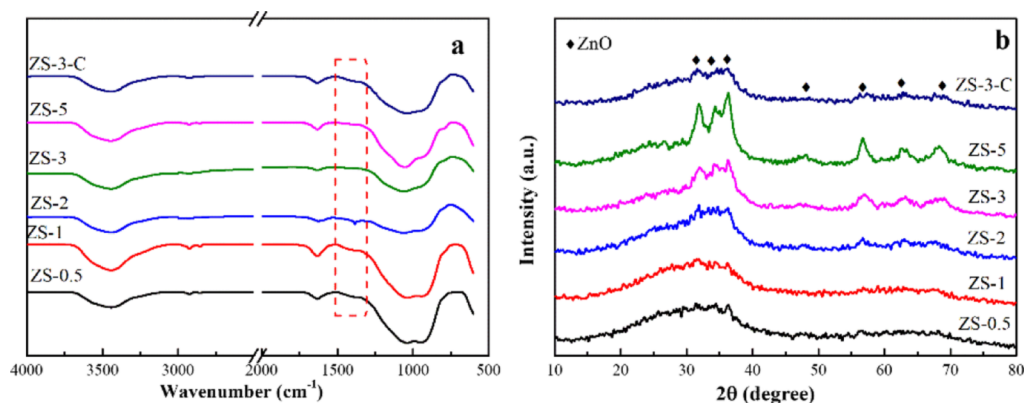
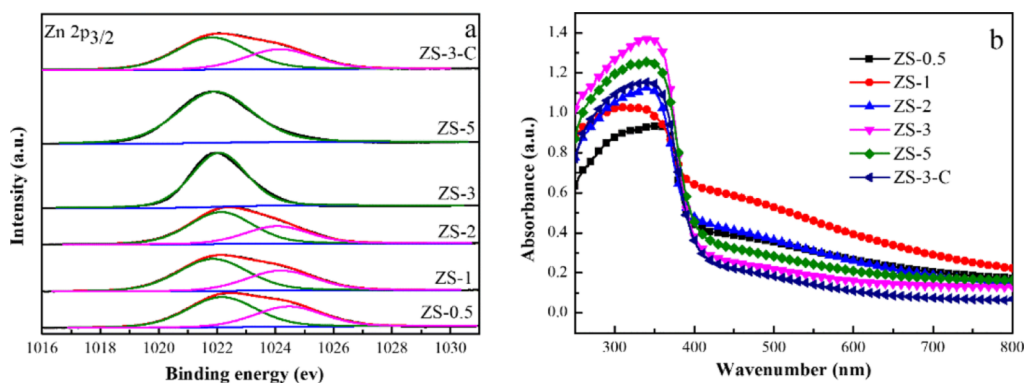**Figure 4.** FT-IR spectrums (a) and XRD patterns (b) of the samples.

Figure 5. XPS spectra of Zn 2p$_{3/2}$ and UV−vis spectra for ZS-X samples.

illustrated that the conventional drying method or reducing the EG content in the precursors favor the decrease of ZnO crystalline sizes, which was consistent with the TEM results. In addition, the characteristic halo of amorphous SiO_2 at $2\theta \approx 23°$ were observed in all samples. However, unlike the results observed in the FT-IR spectrum, no diffraction peaks related to carbonates could be found in the XRD spectra.

XPS and UV−Vis Characterizations. In order to identify the phase composition of the nanocomposites, high resolution XPS spectra of Zn 2p$_{3/2}$ were collected and are shown in Figure 5a. ZS-3 and ZS-5 highlighted only one peak at the binding energy of 1022.1 eV, which was assigned to the characteristic of ZnO.[37,38] Although ZS-3-C, ZS-0.5, ZS-1, and ZS-2 featured an additional peak at about 1024.7 eV, which suggested that two different zinc species with divalent oxidation states were formed in these samples. The latter (1024.7 eV) showed a positive shift (3.6 eV) in comparison with the former (1021.1 eV), indicating a decrease in the outer electron cloud density of Zn^{2+}. Such behavior was observed by Tkachenko et al. and Mei et al., and they ascribed the peak with the higher binding energy to ZnO_x.[39,40] However, no further evidence in this study confirmed the formation of a ZnO_x species. According to the FT-IR results showed in Figure 4a, this peak was confirmed to be related to the monodentate $ZnCO_3$ species. Such similar species was also found in the preparation of CeO_2.[35] The formed monodentate $ZnCO_3$ originated from the coordination of CO_2 molecules with surface defect sites (such as steps, kinks, and edges),[41,42] the needed CO_2 molecules were produced by the decomposition of the precursors during calcination. The amount of monodentate $ZnCO_3$ species quantified from greatest to

least: ZS-0.5 > ZS-1 > ZS-2 > ZS-3-C, and finally, nonexistent in ZS-3 and ZS-5. This can be attributed to ZS-0.5, ZS-1, ZS-2, and ZS-3-C expressing a narrow, average pore size compared to that of ZS-3 and ZS-5 (shown in Figure 3b). More specifically, the produced molecular CO_2 during calcination was hindered in its diffusion, and consequently, coordinated with surface defect sites to form a monodentate $ZnCO_3$ species. The samples with smaller ZnO grain sizes resulted in more surface defect sites, thus more monodentate $ZnCO_3$ species were produced.

The amount of ZnO in the fabricated samples was further determined by the UV−vis spectra (Figure 5b). The absorbance band observed at around 360 nm corresponds to the characteristic ZnO phase, and its intensity can be related to the concentration of ZnO.[39,43] Clearly, the concentration of ZnO was found highest in ZS-3, then gradually decreased in order of ZS-5 > ZS-3-C > ZS-2 > ZS-1 > ZS-0.5. This trend was in agreement with the XPS results. Notably, ZS-5 showed concentrations of ZnO lower than those of ZS-3, which was because of the larger ZnO grains and inhomogenous dispersion.[44]

From the above characterizations, the breakthrough results could be readily interpreted that although the samples, ZS-3-C, ZS-0.5, ZS-1, and ZS-2, possessed smaller ZnO grains, the generation of monodentate $ZnCO_3$ species on the ZnO surface inhibited the reaction between ZnO and H_2S, thereby resulting in lower sulfur capacities than that of ZS-3. This observation was verified by ZS-0.5 forming the largest amount of monodentate $ZnCO_3$ species and exhibiting the lowest sulfur capacity (28.6 mg S/g sorbent). By reducing the amount of the $ZnCO_3$ species, ZS-1 and ZS-2 showed an improvement in the

BSCs. ZS-3 and ZS-5 had a pure ZnO phase according to the XPS results, and therefore, demonstrated a higher sulfur capacity. In addition, because of the smaller ZnO grains in ZS-3 than that in ZS-5, ZS-3 manifested a sulfur capacity higher than that of ZS-5.

Insight of the Mechanism Involved in the New Sol−Gel Strategy. Based on the above description, the drying method and the molar ratio of EG/nitrates are key to successfully preparing high efficient ZnO/SiO_2 adsorbents using the new sol−gel strategy. In order to understand how these two parameters influence the physicochemical properties of the fresh composites, the characterizations of gels before calcination were carried out.

Figure 6 shows the FT-IR spectra of the gels before calcination. Clearly, all of the gels produced the SiO_2
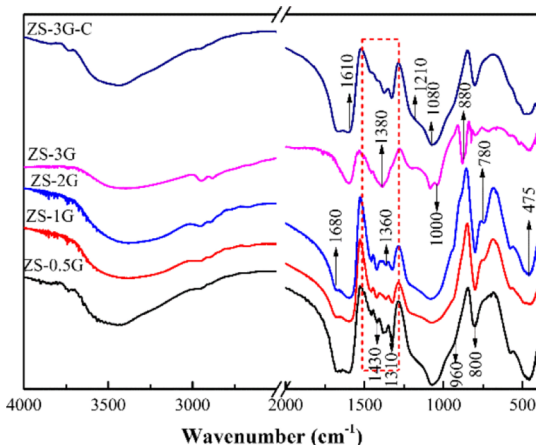

Figure 6. The FT-IR spectra of gels before calcination.

characteristic adsorption bands at 475, 800, 1080, and 1210 cm^{-1}, as depicted in Figure 4a. This indicates that the TEOS had hydrolyzed and cross-linked to the SiO_2 networks during the drying process. In addition, the Si−OH band at 960 cm^{-1},[11] and the adsorption bands of −OH groups at 1610 cm^{-1} (deforming vibrations) and 3440 cm^{-1} (stretching vibrations)[34] are also present in all gels.

Contrasted with ZS-3G, ZS-3G-C showed no characteristic peak of NO_3^- ion centered at 1380 cm^{-1}[45] but presented some new adsorption bands, such as $\nu_s(CO)$ at 1311 cm^{-1}, $\delta(OH)$ at 1360 cm^{-1}, $\nu_s(COO)$ at 1430 cm^{-1}, $\nu_{as}(COO)$ at 1680 cm^{-1},[22,34,46] as well as the characteristic $\delta(OCO) + \nu(MO)$ vibration peak at 780 cm^{-1}.[25,34] These newly appeared adsorption bands suggest that the redox reaction between EG and nitrates occurred and formed carboxylate complex using the conventional drying method during the gels drying process, which was consistent with other literature.[22,46−48] Interestingly, these similar results were obtained when modulating the molar ratio of EG/nitrates ≤ 2 in the new developed strategy. Besides NO_3^- at 1380 cm^{-1}, ZS-3G also produced an additional peak at 880 cm^{-1} corresponding to the vibration of $\delta(CH_2)$ in EG,[22] which confirms the presence of NO_3^- and EG in ZS-3G. Consequently, these results suggest that the redox reaction between EG and nitrates actually did not occur in ZS-3G. More importantly, it was found that the absorption band at 3440 cm^{-1}, attributing to the OH groups in ZS-3G, became weaker and broader in comparison to that of the other gels. Furthermore, the wavenumber of Si−OH band red shifted from 960 to 1000 cm^{-1}, which strongly

demonstrates the formation of hydrogen bonds between EG and silanol or between EG and H_2O within the gels.[49,50] Therefore, the rationale for the lack of redox reaction in ZS-3G is reasonable: the innovative drying method and proper molar ratio of EG/nitrates favor the formation of hydrogen bonds in the gels during the drying process, which deterred the oxidation of EG by nitrates under similar conditions.

Figure 7 shows the thermogravimetry (TG)−mass spectrometry (MS) results of the gels during heat treatment. Figure 7a shows that ZS-3G-C lost a total weight of 31%, which is far less than that in ZS-3G (59%). According to the previous FT-IR results (Figure 6), this was caused by the redox reaction between EG and nitrates in ZS-3G-C during the gel-drying process. ZS-0.5 G, ZS-1G, and ZS-2G showed similar total weight loss percentages averaging 28%. From derivative thermogravimetry (DTG) results showed in Figure 7b, two main weight loss peaks centered at 100 and 350 °C were observed in ZS-3-C, ZS-0.5, ZS-1, and ZS-2, demonstrating similar thermal behaviors from these samples. The first significant weight loss in the gel samples occurred at 100 °C, which can be ascribed to the evaporation of the physically adsorbed water. The second significant weight loss was observed at 350 °C, which represents the evolution of large amounts of CO_2 and water, originating from the decomposition of carboxylate.[22,46]

ZS-3G and ZS-5G revealed more complex thermal behaviors than those of the above gels. More specifically, both gels produced three weight loss peaks noted at 140, 155, and 350 °C. Because of the release of large amounts of gases, such as CO_2, NO_2, and H_2O, the first two peaks were considered to be the result of auto-combustion of EG and NO_3^- on the surface and in the pore channels of the silica gels, respectively.[35,51] Comparatively, ZS-3G released less gas compounds (CO_2, NO_2, and H_2O) at 140 °C than at 155 °C, whereas ZS-5G released more gases at 140 °C than at 155 °C. These results demonstrate that more zinc nitrates and EG in ZS-5G were enriched on the surface of SiO_2 rather than being embedded in the SiO_2 matrix. This affirms the results of TEM, where a phase isolation was observed in ZS-5. The peaks at 350 °C can be attributed to the decomposition of the carboxylate species, which was generated by the incomplete combustion of EG and nitrates at the earlier stage.

Based on the FT-IR and TG−MS results, although the developed preparation strategy in this article used the similar precursors system (EG−metallic nitrates−TEOS) as that in ref 22, the involved formation mechanism of ZnO nanograins was completely different. In the previous work, ZnO nanograins were formed by the decomposition of the intermediate carboxylate complex, which was produced through the redox reaction between nitrates and EG during the drying process. Whereas in our strategy, ZnO nanograins was formed by the auto-combustion of EG and nitrates, wherein EG is not solely used as a modifier to form a developed mesoporous SiO_2 matrix during the gel drying process, but also as a fuel to promote the decomposition of nitrates and increase the surface area of the composites during calcination. In a word, a new sol−gel strategy for the preparation of ZnO/SiO_2 adsorbents was developed by modifying a gel-drying method and simultaneously controlling ZnO-grain formation through optimizing the molar ratio of EG/nitrates in its precursors.

Facility and Versatility of This Strategy. Considering the facility of the designed sol−gel method, the sample ZS-3 with different solvents (W: H_2O, M: CH_3OH, E: CH_3CH_2OH,
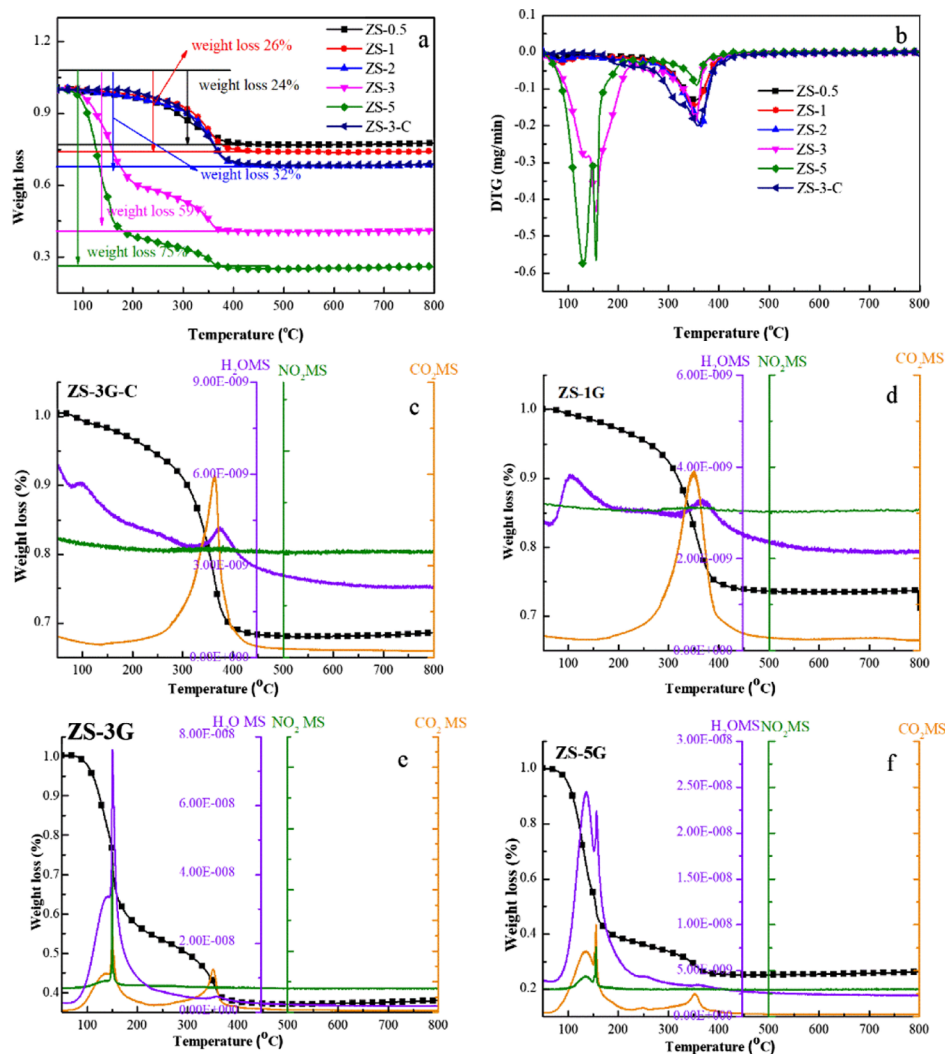
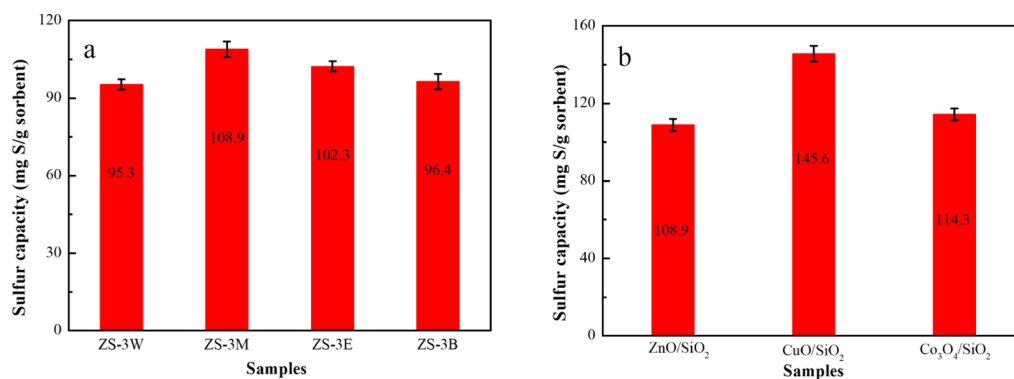**Figure 7.** TG (a), DTG (b), and TG−MS (c−f) of the gels after overnight drying at 120 °C.

Figure 8. The BSCs of the samples.

and B: $CH_3(CH_2)_3OH$) were synthesized and will be denoted as ZS-3-Y, where Y is the type of solvent used in the $Zn(NO_3)_2$ preparation. The H_2S removal performance was measured, and the results are shown in Figure 8a. An insignificant decrease in the H_2S removal capacity was observed after changing the type of solvent, illustrating the facility of this strategy. The versatility of this method was also evidenced by the preparation of other metal oxide/SiO_2 adsorbents, such as CuO/SiO_2 and Co_3O_4/SiO_2 sorbents; their adsorption results are shown in Figure 8b.

The CuO/SiO_2 and Co_3O_4/SiO_2 sorbents displayed high BSCs with 145.6 mg S/g sorbent and 114.3 mg S/g sorbent, respectively.

The H_2S removal performance of the sample was also compared to the reported results prepared by different methods, and the corresponding results are shown in Table 3. Clearly, the designed strategy in this work highlights many advantages, such as greater M_xO_y loadings, BSCs, and even M_xO_y utilizations. Notably, the BSCs improved an order of

Table 3. Comparison of BSCs of M$_x$O$_y$-Based Sorbents with Those Reported in the Literature

samples	preparation methods	optimal loading (wt %)	BSCs (mg/g)	utilization (%)	references
Z30/K6	incipient wetness	30	37.6	31.9	12
ZnO/SBA-15-F	incipient wetness	15	21.8	36.3	26
ZnO/SiO$_2$	sol−gel	30	90.7	76.9	9
3D-SZ50-500	colloidal crystal template	50	135	69	11
ZS-3	sol−gel	57.6	108.9	48.1	this work
20Cu/MSU-1	incipient wetness	20	18.3	19	52
CuO-C-EPM	commercialization	80	27	8.4	53
3DOM-SC-43	colloidal crystal template	43	147	73.5	54
CuO/SiO$_2$	sol−gel	57.1	145.6	63.4	this work
M-Co-250	inverse micelle soft template	100	134	25.2	55
3D-SCE57-500	colloidal crystal template	57	189	63.0	56
CoOOH/GO-10	precipitation and oxidation	90	101.8		57
Co$_3$O$_4$/SiO$_2$	sol−gel	57.2	114.3	37.6	this work

magnitude through this method compared with those prepared by the incipient wetness method. To conclude, this sol−gel strategy demonstrates promising potential in desulfurization due to its facility, versatility, and high efficiency.

CONCLUSIONS

In summary, a facile and versatile sol−gel method for the preparation of highly loaded ZnO/SiO$_2$ nanocomposites was designed using TEOS−EG−nitrates as the precursors. The crucial step in this methodology is the innovative drying method and the ability to control the ZnO formation mechanism by modulating the molar ratio of EG/nitrates in the precursors. While modulating the molar ratio of EG/nitrates ≥ 3, EG is not solely used as modifier to form a developed mesoporous SiO$_2$ matrix by inhibiting the crosslink of hydrolyzed silanol during the gel drying process, but also as a fuel to promote the decomposition of nitrates and increase the surface area of the composites during calcination. Such fabricated adsorbent possessed both well-dispersed ZnO nanograins and high ZnO loadings (57 wt %), resulting in a high H$_2$S removal capacity of 108.9 mg S/g sorbent. Contrastingly, the conventional drying method or modulating the molar ratio of EG/nitrates ≤ 2 favor a redox reaction between EG and nitrates, which form intermediate carboxylate species during the gel drying process. Although the formed ZnO grains were less than 5 nm in the subsequent calcination, monodentate ZnCO$_3$ impurities were formed and covered the ZnO surface, which greatly decreases the reactivity of ZnO toward H$_2$S. Finally, the fabricated CuO/SiO$_2$ and Co$_3$O$_4$/SiO$_2$ sorbents displayed high BSCs with 145.6 and 114.3 mg S/g sorbent, respectively, confirming the versatility and high efficiency of this method.

AUTHOR INFORMATION

Corresponding Author
*E-mail: fanhuiling@tyut.edu.cn
ORCID
Huiling Fan: 0000-0001-8616-6578
Notes
The authors declare no competing financial interest.

ACKNOWLEDGMENTS

REFERENCES

(1) Zhang, J.; Wang, H.; Wilkinson, D. P.; Song, D.; Shen, J.; Liu, Z.-S. Model for the contamination of fuel cell anode catalyst in the presence of fuel stream impurities. *J. Power Sources* **2005**, *147*, 58−71.

(2) Cheng, X.; Shi, Z.; Glass, N.; Zhang, L.; Zhang, J.; Song, D.; Liu, Z.-S.; Wang, H.; Shen, J. A review of PEM hydrogen fuel cell contamination: Impacts, mechanisms, and mitigation. *J. Power Sources* **2007**, *165*, 739−756.

(3) Parks, S. M.; Obrien, T. J. *Effects of Several Trace Contaminants on Fuel Cell Performance*. Morgantown Energy Research Center 1980.

(4) Wang, Z.; Du, W.; Wang, J.; Zhou, J.; Han, X.; Zhang, Z.; Huang, L. Research and application of improved adaptive MOMEDA fault diagnosis method. *Measurement* **2019**, *140*, 63−75.

(5) Wang, Z.; Zhou, J.; Wang, J.; Du, W.; Wang, J.; Han, X.; He, G. A novel fault diagnosis method of gearbox based on maximum kurtosis spectral entropy deconvolution. *IEEE Access* **2019**, *7*, 29520−29532.

(6) Mohtadi, R.; Lee, W.-k.; Cowan, S.; Van Zee, J. W.; Murthy, M. Effects of hydrogen sulfide on the performance of a PEMFC. *Electrochem. Solid-State Lett.* **2003**, *6*, A272.

(7) Shi, W.; Yi, B.; Hou, M.; Jing, F.; Yu, H.; Ming, P. The influence of hydrogen sulfide on proton exchange membrane fuel cell anodes. *J. Power Sources* **2007**, *164*, 272−277.

(8) Gould, B. D.; Baturina, O. A.; Swider-Lyons, K. E. Deactivation of Pt/VC proton exchange membrane fuel cell cathodes by SO$_2$, H$_2$S and COS. *J. Power Sources* **2009**, *188*, 89−95.

(9) Liu, G.; Huang, Z.-H.; Kang, F. Preparation of ZnO/SiO$_2$ gel composites and their performance of H$_2$S removal at room temperature. *J. Hazard. Mater.* **2012**, *215−216*, 166−172.

(10) Yang, C.; Wang, J.; Fan, H.-L.; Shangguan, J.; Mi, J.; Huo, C. Contributions of tailored oxygen vacancies in ZnO/Al$_2$O$_3$ composites to the enhanced ability for H$_2$S removal at room temperature. *Fuel* **2018**, *215*, 695−703.

(11) Wang, L.-J.; Fan, H.-L.; Shangguan, J.; Croiset, E.; Chen, Z.; Wang, H.; Mi, J. Design of a sorbent to enhance reactive adsorption of hydrogen sulfide. *ACS Appl. Mater. Interfaces* **2014**, *6*, 21167−21177.

(12) Li, L.; Sun, T. H.; Shu, C. H.; Zhang, H. B. Low temperature H$_2$S removal with 3-D structural mesoporous molecular sieves supported ZnO from gas stream. *J. Hazard. Mater.* **2016**, *311*, 142−150.

(13) Baird, T.; Denny, P. J.; Hoyle, R.; McMonagle, F.; Stirling, D.; Tweedy, J. Modified zinc oxide absorbents for low-temperature gas desulfurization. *J. Chem. Soc. Faraday. Trans.* **1992**, *88*, 3375−3382.

(14) Samokhvalov, A.; Tatarchuk, B. J. Characterization of active sites, determination of mechanisms of H$_2$S, COS and CS$_2$ sorption and regeneration of ZnO low-temperature sorbents: past, current and perspectives. *Phys. Chem. Chem. Phys.* **2011**, *13*, 3197−3209.

(15) Shah, M. S.; Tsapatsis, M.; Siepmann, J. I. Hydrogen sulfide capture: from absorption in polar liquids to oxide, zeolite, and metal-organic framework adsorbents and membranes. *Chem. Rev.* **2017**, *117*, 9755−9803.

(16) Vargas, D. X. M.; De la Rosa, J. R.; Lucio-Ortiz, C. J.; Hernández-Ramirez, A. Photocatalytic degradation of trichloro-ethylene in a continuous annular reactor using Cu-doped TiO_2 catalysts by sol−gel synthesis. *Appl. Catal., B* **2015**, *179*, 249−261.

(17) Riyapan, S.; Boonyongmaneerat, Y.; Mekasuwandumrong, O.; Praserthdam, P.; Panpranot, J. Effect of surface Ti^{3+} on the sol−gel derived TiO_2 in the selective acetylene hydrogenation on Pd/TiO_2 catalysts. *Catal. Today* **2015**, *245*, 134−138.

(18) Zhao, C.; Zhou, Z.; Cheng, Z.; Fang, X. Sol-gel-derived, $CaZrO_3$-stabilized $Ni/CaO-CaZrO_3$ bifunctional catalyst for sorption-enhanced steam methane reforming. *Appl. Catal., B* **2016**, *196*, 16−26.

(19) Polychronopoulou, K.; Fierro, J. L. G.; Efstathiou, A. M. Novel Zn−Ti-based mixed metal oxides for low-temperature adsorption of H_2S from industrial gas streams. *Appl. Catal, B* **2005**, *57*, 125−137.

(20) Polychronopoulou, K.; Efstathiou, A. M. Effects of sol-gel synthesis on 5Fe-15Mn-40Zn-40Ti-O mixed oxide structure and its H_2S removal efficiency from industrial gas streams. *Environ. Sci. Technol.* **2009**, *43*, 4367−4372.

(21) Polychronopoulou, K.; Fierro, J. L. G.; Efstathiou, A. M. Novel Zn-Ti-based mixed metal oxides for low-temperature adsorption of H_2S from industrial gas streams. *Appl. Catal., B* **2005**, *57*, 125−137.

(22) Stefanescu, M.; Caizer, C.; Stoia, M.; Stefanescu, O. Ultrafine, perfectly spherical Ni-Zn ferrite nanoparticles, with ultranarrow distribution, isolated in a silica matrix, prepared by a novel synthesis method in the liquid phase. *Acta Mater.* **2006**, *54*, 1249−1256.

(23) Stefanescu, M.; Stoia, M.; Caizer, C.; Stefanescu, O. Preparation of $x(Ni_{0.65}Zn_{0.35}Fe_2O_4)/(100−x)SiO_2$ nanocomposite powders by a modified sol−gel method. *Mater. Chem. Phys.* **2009**, *113*, 342−348.

(24) Sun, Y.; Yin, Y.; Mayers, B. T.; Herricks, T.; Xia, Y. Uniform silver nanowires synthesis by reducing $AgNO_3$ with ethylene glycol in the presence of seeds and poly(vinyl pyrrolidone). *Chem. Mater.* **2002**, *14*, 4736−4745.

(25) Ştefănescu, M.; Ştefănescu, O.; Stoia, M.; Lazau, C. Thermal decomposition of some metal-organic precursors. *J. Therm. Anal. Calorim.* **2007**, *88*, 27−32.

(26) Hussain, M.; Abbas, N.; Fino, D.; Russo, N. Novel mesoporous silica supported ZnO adsorbents for the desulphurization of biogas at low temperatures. *Chem. Eng. J.* **2012**, *188*, 222−232.

(27) Ullah, R.; Bai, P.; Wu, P.; Zhang, Z.; Zhong, Z.; Etim, U. J.; Subhan, F.; Yan, Z. Comparison of the reactive adsorption desulfurization performance of $Ni/ZnO-Al_2O_3$ adsorbents prepared by different methods. *Energy Fuels* **2016**, *30*, 2874−2881.

(28) Higginbotham, C. P.; Browner, R. F.; Jenkins, J. D.; Rice, J. K. Dependence of drying technique on surface area and pore size for polyethylene glycol/tetramethoxysilicate hybrid gels. *Mater. Lett.* **2003**, *57*, 3970−3975.

(29) Ågren, P.; Pendleton, P.; Rosenholm, J. B. Microstructural analysis of the effects of poly(ethylene glycol) on an acid catalyzed sol-gel derived ceramic material. *Adsorption* **1999**, *5*, 305−312.

(30) Stefanescu, M.; Stoia, M.; Stefanescu, O. Thermal and FT-IR study of the hybrid ethylene-glycol-silica matrix. *J. Sol-Gel Sci. Technol.* **2006**, *41*, 71−78.

(31) Uchida, N.; Ishiyama, N.; Kato, Z.; Uematsu, K. Chemical effects of DCCA to the sol-gel reaction process. *J. Mater. Sci.* **1994**, *29*, 5188−5192.

(32) Yang, H.; Xiao, Y.; Liu, K.; Feng, Q. Chemical precipitation synthesis and optical properties of ZnO/SiO_2 nanocomposites. *J. Am. Ceram. Soc.* **2008**, *91*, 1591−1596.

(33) Rao, A. V.; Wagh, P. B. Preparation and characterization of hydrophobic silica aerogels. *Bull. Chin. Ceram. Soc.* **2008**, *53*, 13−18.

(34) Stefanescu, M.; Stoia, M.; Stefanescu, O. Ni,Zn/SiO_2 ferrite nanocomposites prepared by an improved sol-gel method and their characterisation. *J. Optoelectron. Adv. Mater.* **2005**, *7*, 607−614.

(35) Chen, W.; Li, F.; Yu, J. Combustion synthesis and characterization of nanocrystalline CeO_2-based powders via ethylene glycol-nitrate process. *Mater. Lett.* **2006**, *60*, 57−62.

(36) Yang, C.; Wang, J.; Fan, H.; Hu, Y.; Shen, J.; Shangguan, J.; Wang, B. Activated Carbon-Assisted Fabrication of Cost-Efficient ZnO/SiO_2 Desulfurizer with Characteristic of High Loadings and High Dispersion. *Energy Fuels* **2018**, *32*, 6064−6072.

(37) Wu, X.; Wen, L.; Lv, K.; Deng, K.; Tang, D.; Ye, H.; Du, D.; Liu, S.; Li, M. Fabrication of ZnO/graphene flake-like photocatalyst with enhanced photoreactivity. *Appl. Surf. Sci.* **2015**, *358*, 130−136.

(38) Feng, Y.; Mi, J.; Wu, M.; Shangguan, J.; Fan, H. In Situ Preparation and Regeneration Behaviors of Zinc Oxide/Red Clay Desulfurization Sorbents. *Energy Fuels* **2016**, *31*, 1015−1022.

(39) Tkachenko, O. P.; Klementiev, K. V.; Löffler, E.; Ritzkopf, I.; Schüth, F.; Bandyopadhyay, M.; Grabowski, S.; Gies, H.; Hagen, V.; Muhler, M.; Lu, L.; Fischer, R. A.; Grünert, W. The structure of zinc and copper oxide species hosted in porous siliceous matrices. *Phys. Chem. Chem. Phys.* **2003**, *5*, 4325−4334.

(40) Mei, B.; Becerikli, A.; Pougin, A.; Heeskens, D.; Sinev, I.; Grünert, W.; Muhler, M.; Strunk, J. Tuning the acid/base and structural properties of titanate-loaded mesoporous silica by grafting of zinc oxide. *J. Phys. Chem. C* **2012**, *116*, 14318−14327.

(41) Noei, H.; Wöll, C.; Muhler, M.; Wang, Y. Activation of carbon dioxide on ZnO nanoparticles studied by vibrational spectroscopy. *J. Phys. Chem. C* **2010**, *115*, 908−914.

(42) Gankanda, A.; Cwiertny, D. M.; Grassian, V. H. Role of atmospheric CO_2 and H_2O adsorption on ZnO and CuO nanoparticle aging: formation of new surface phases and the impact on nanoparticle dissolution. *J. Phys. Chem. C* **2016**, *120*, 19195−19203.

(43) Ullah, R.; Zhang, Z.; Bai, P.; Wu, P.; Han, D.; Etim, U. J.; Yan, Z. One-pot cation−anion double hydrolysis derived $Ni/ZnO−Al_2O_3$ absorbent for reactive adsorption desulfurization. *Ind. Eng. Chem. Res.* **2016**, *55*, 3751−3758.

(44) Kato, H.; Nakamura, A.; Takahashi, K.; Kinugasa, S. Size effect on UV-Vis absorption properties of colloidal C60 particles in water. *Phys. Chem. Chem. Phys.* **2009**, *11*, 4946−4948.

(45) Castro, P. M.; Jagodzinski, P. W. FTIR and Raman spectra and structure of $Cu(NO_3)^+$ in aqueous solution and acetone. *Spectrochim. Acta, Part A* **1991**, *47*, 1707−1720.

(46) Ştefănescu, M.; Sasca, V.; Bîrzescu, M. Studies on the thermal decompositions of heteropolynuclear glyoxylates of Cr(III) and Cu(II). *J. Therm. Anal. Calorim.* **1999**, *56*, 579−586.

(47) Sadakane, M.; Asanuma, T.; Jun, K.; Ueda, W. Facile procedure to prepare three-dimensionally ordered macroporous (3DOM) perovskite-type mixed metal oxides by colloidal crystal templating method. *Chem. Mater.* **2005**, *17*, 3546−3551.

(48) Stefănescu, M.; Sasca, V.; Bîrzescu, M. Thermal behaviour of the homopolynuclear glyoxylate complex combinations with Cu(II) and Cr(III). *J. Therm. Anal. Calorim.* **2003**, *72*, 515−524.

(49) Hao, L.; Su, T.; Hao, D.; Deng, C. Oxidative desulfurization of diesel fuel with caprolactam-based acidic deep eutectic solvents: Tailoring the reactivity of DESs by adjusting the composition. *Chin. J. Catal.* **2018**, *39*, 1552−1559.

(50) Mizuno, K.; Miyashita, Y.; Shindo, Y.; Ogawa, H. NMR and FT-IR studies of hydrogen bonds in ethanol-water mixtures. *J. Phys. Chem.* **1995**, *99*, 3225−3228.

(51) Chen, W.; Li, F.; Liu, L.; Li, Y. Synthesis of nano-sized yttria via a sol-gel process based on hydrated yttrium nitrate and ethylene glycol and its catalytic performance for thermal decomposition of NH_4ClO_4. *J. Rare Earths* **2006**, *24*, 543−548.

(52) Montes, D.; Tocuyo, E.; González, E.; Rodríguez, D.; Solano, R.; Atencio, R.; Ramos, M. A.; Moronta, A. Reactive H_2S chemisorption on mesoporous silica molecular sieve-supported CuO or ZnO. *Microporous Mesoporous Mater.* **2013**, *168*, 111−120.

(53) Mabayoje, O.; Seredych, M.; Bandosz, T. J. Enhanced reactive adsorption of hydrogen sulfide on the composites of graphene/graphite oxide with copper (hydr)oxychlorides. *ACS Appl. Mater. Interfaces* **2012**, *4*, 3316−3324.

(54) Wang, J.; Wang, L.; Fan, H.; Wang, H.; Hu, Y.; Wang, Z. Highly porous copper oxide sorbent for H$_2$S capture at ambient temperature. *Fuel* **2017**, *209*, 329−338.

(55) Pahalagedara, L. R.; Poyraz, A. S.; Song, W.; Kuo, C.-H.; Pahalagedara, M. N.; Meng, Y.-T.; Suib, S. L. Low temperature desulfurization of H$_2$S: high sorption capacities by mesoporous cobalt oxide via increased H$_2$S diffusion. *Chem. Mater.* **2014**, *26*, 6613−6621.

(56) Wang, J.; Yang, C.; Zhao, Y.-R.; Fan, H.-L.; Wang, Z.-D.; Shangguan, J.; Mi, J. Synthesis of Porous Cobalt Oxide and Its Performance for H$_2$S Removal at Room Temperature. *Ind. Eng. Chem. Res.* **2017**, *56*, 12621−12629.

(57) Florent, M.; Bandosz, T. J. Effects of surface heterogeneity of cobalt oxyhydroxide/graphite oxide composites on reactive adsorption of hydrogen sulfide. *Microporous Mesoporous Mater.* **2015**, *204*, 8−14.